# Chapter 7
# Characteristic Features of Deformation and Fracture in Hydrogen Embrittlement

In Chap. 6, the degradation of mechanical properties that appear at various testing methods in the presence of hydrogen is described. An issue to be followed is features that characterize deformation and fracture behaviors common to various testing methods originating in functions of hydrogen. Fracture of materials proceeds macroscopically starting from the nucleation and growth of crack, and each stage exhibits features varying by materials and situations such as stress states and environments. The features are diverse but are closely related to underlying mechanisms of deformation and fracture. The comprehensive understanding of commonness in hydrogen effects is useful for revealing intrinsic mechanism and also to judge the origins of service failure.

## 7.1 Fractographic Features

Fracture surface exhibits the crack propagation path. Since plastic deformation dissipates the major part of the energy needed for crack propagation, the concern of plasticity is an important aspect in examining fracture surfaces. Fracture surfaces of metallic materials are diverse depending on situations but are classified into a few basic modes: cleavage, interface separation and microvoid coalescence. Fracture surfaces of hydrogen-degraded steels exhibit some characteristic features depending on microstructures, hydrogen concentration or fugacity, and stress states. However, the basic classification of fracture modes is not exceptional for hydrogen embrittlement, and characteristic features due to hydrogen are to be examined in the framework of the basic modes of fracture und their underlying mechanisms.

(a) Cleavage

Cleavage fracture is typical for brittle fracture of body-centered-cubic steels and is characterized by the transgranular crack propagation along {100} planes



M. Nagumo, *Fundamentals of Hydrogen Embrittlement*,
DOI 10.1007/978-981-10-0161-1_7

associated with river markings. For hydrogen embrittlement of steels, cleavage fracture is exceptional and appears when an incipient crack is formed by the precipitation of molecular hydrogen of a high fugacity that satisfies the Griffith condition for unstable crack extension. Cleavage fracture was observed for Fe-3% Si single crystals which were severely hydrogen-charged either by cathodic electrolysis in a 4 vol.% $H_2SO_4 + CS_2 + As_2O_3$ solution at a current density of 160 A/m$^2$ or by quenching from a hydrogen atmosphere of 0.125 MPa at 700 ~ 1200 °C [1]. While the specimens were not externally loaded, the arrays of decorated dislocations in the vicinity of cracks indicated plastic deformation associated with discontinuous growth of cracks. On the other hand, under combined static loading and hydrogen charging, *i.e.* in sustained-loading delayed fracture tests, fracture surfaces exhibited a large number of curved steps different from cleavage steps [2].

Cleavage fracture in hydrogen embrittlement was also observed on the tensile test of 0.014%C iron single crystal at room temperature under simultaneous hydrogen charging [3]. The tensile axis was along [001] axis, and hydrogen was charged by cathodic electrolysis in poisoned 0.05 N $H_2SO_4$ at a current density of over 30 A/m$^2$. In that case, cleavage fracture with river markings took place after the crack advance with striation-like appearance. Details of striation-like appearance are described in Sect. 7.1(c).

(b) Dimple patterns

Dimple patterns typically characterize ductile fracture that proceeds with the so-called microvoid coalescence (MVC). The size and shape of dimples are not uniform and are roughly classified into relatively large primary dimples and fine secondary ones. Second phase particles are often observed accompanying primary dimples, but fine secondary dimples without any particles are commonly observed.

Dimple patterns appear on hydrogen-assisted fracture surfaces of steels in cases where a substantial ductility still remains in degradation. An increase in dimple size by hydrogen precharging was reported for tensile fracture of spheroidized near-eutectoid steels [4]. In that case, diameters and spacing of carbides were less than or comparable to dimple size. Hydrogen precharging was conducted under a fairly high fugacity using cathodic electrolysis in 1 N $H_2SO_4$ poisoned by arsenic at a current density as large as 300 A/m$^2$. High hydrogen fugacity of precipitated hydrogen should have promoted void formation by causing separation of the interface between carbides and surrounding matrix. On the other hand, hydrogen generally reduces the size of secondary dimples. On a mixed mode I/III loading fracture toughness test of a high purity Ni-Cr-Mo-V steel of lower bainitic structure of 855 MPa in tensile strength, hydrogen precharging at an equivalent hydrogen fugacity of 1.26 MPa at room temperature degraded the fracture toughness associated with reduced dimple sizes compared with those of uncharged specimens [5].

The fracture surface at a three-point bending test of a mildly hydrogen-precharged low-carbon medium strength steel exhibited patterns consisting of mostly primary and secondary dimples [6]. Hydrogen precharging caused rather enlargement of primary dimples while secondary dimples were refined. The area fractions of dimples with different depth ($h$)/width ($w$) ratio are shown

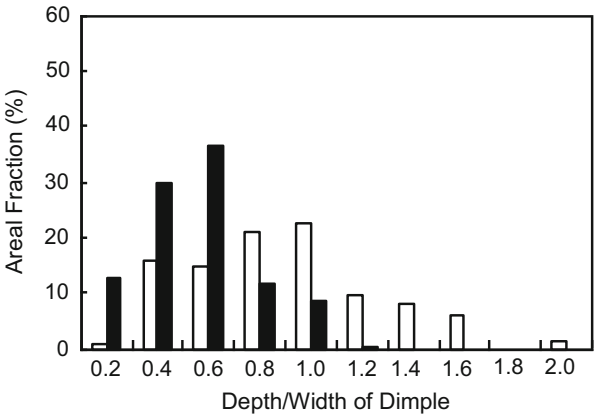


**Fig. 7.1** Area fractions of dimples with different depth/width ratio on fracture surfaces of a low-carbon medium strength steel subjected to a three-point bending test with/without hydrogen precharging. The open and filled bars indicate non-charged and hydrogen-charged specimens, respectively (Nagumo et al. [6])

in Fig. 7.1 [6] for hydrogen precharged and uncharged specimens. The area fraction of shallow dimples ($h/w < 0.5$) increased by hydrogen precharging. It implies that hydrogen reduces the extent of plastic deformation on dimple formation and thus the energy dissipated during ductile crack propagation.

Shallow dimples are generally observed in cases of moderate degradation as a characteristic feature of hydrogen embrittlement. Examples are found for low alloy steel in three-point bending test [7] and Type 304 austenitic stainless steel in tensile test [8]. For as-quenched low carbon martensitic steel subjected to tensile tests, an orientation relationship of the fracture surface that exhibited dimple patterns was parallel to $\{011\}_M$ planes which are also parallel to block and lath boundaries of martensite [9]. In that case, microcracks along prior austenite grain boundaries were observed in areas far from the fracture surface. Hydrogen precharging was conducted by cathodic electrolysis in 1 N $H_2SO_4$ with $As_2O_3$ at a current density of 100 A/m$^2$.

(c) Striations

Striations have been observed mostly for single crystal and coarse-grain specimens. Striations on the tensile fracture surface are shown in Fig. 7.2 [3] for hydrogenated 0.001 % C iron single crystal. The crack growth as a whole was in the [010] direction macroscopically on the (001) plane, but the actual growth of the crack front was in <110> directions. Striations parallel to the crack front were coincident with traces of {112} slip planes. Examinations of fine details by means of scanning tunneling microscopy (STM) and mating of opposite fracture surfaces revealed the formation of fine voids at intersections of striations as shown schematically in the lower part of Fig. 7.2. Crystallographic relations are consistent with the void formation originating in interactions of dislocations that move on intersecting slip planes.

Fine striations of about 1 μm spacing along {112} slip planes were reported formerly associated with the slow crack growth macroscopically on {001} and in <110> directions for Fe-3%Si single crystal specimens [10]. Fatigue-prenotched

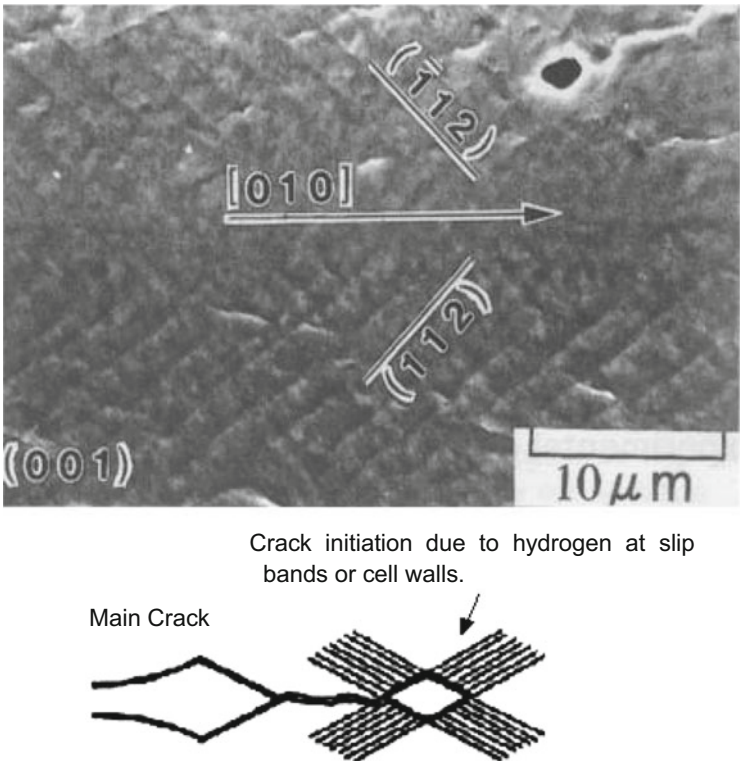


**Fig. 7.2** Striations on the tensile-fracture surface of a hydrogen-charged iron single crystal specimen. The lower illustration is a schematic STM view showing a microcrack formed at the intersection of striations (Terasaki et al. [3])

disc-shaped miniature compact tension specimens were gaseous hydrogen charged and subjected to sustained-loading tests with the loading axis parallel to <110>. Simultaneously conducted acoustic emission (AE) measurements detected discontinuous crack growth. The discontinuous steps were ascribed to intermittent cleavage fracture, but direct evidences for cleavage were not presented from crystallographic measurements.

Fine structures of striations and associated plasticity were examined for the internal surface of hydrogen-induced cracks formed within coarse-grain polycrystalline Fe-3%Si specimens [11]. Internal cracks initiated at non-metallic inclusions and propagated macroscopically on {100} cleavage planes associated with striations of an average spacing of 300 nm. Finer striations with a spacing of around 30 nm and a height of 15 nm were also observed. Transmission electron microscopy (TEM) revealed planar slip with interplanar spacing of 15–30 nm that corresponded to the separation of fine striations. Electron backscatter diffraction (EBSD) patterns from regions within internal cracks were diffuse and indicated a substantial crystalline distortion.

Essentially the same and a more pronounced involvement of plasticity in hydrogen-induced crack growth was observed for pure iron [12]. Hydrogen-induced cracks in a bicrystalline pure iron specimen were formed under a high hydrogen fugacity without applying external stress. The cracks were parallel to variants of mostly {110} and partially to {112}, instead of {001} in the case of Fe-3%Si specimens. Fracture surfaces showing striations with planar segments and markings perpendicular to the advancing crack front were common to Fe-3%Si specimens. Planar segments perpendicular to primary striations were also parallel to variants of slip planes.

Above findings indicate that the growth of internal cracks induced by hydrogen is associated with a substantial plasticity even though the appearance is macroscopically brittle-like. A crucial problem is the role of striations in degradation. The effects of hydrogen will distinctly appear in cases where a substantial plastic deformation is present prior to the final stage of fracture. Figure 7.3 [13] shows a cross-section of a commercial pure iron specimen tensile fractured at room temperature under hydrogen charging by cathodic electrolysis in 3 % NaCl aqueous solution at a current density of 100 A/m$^2$. The specimens of 5 mm in diameter had a

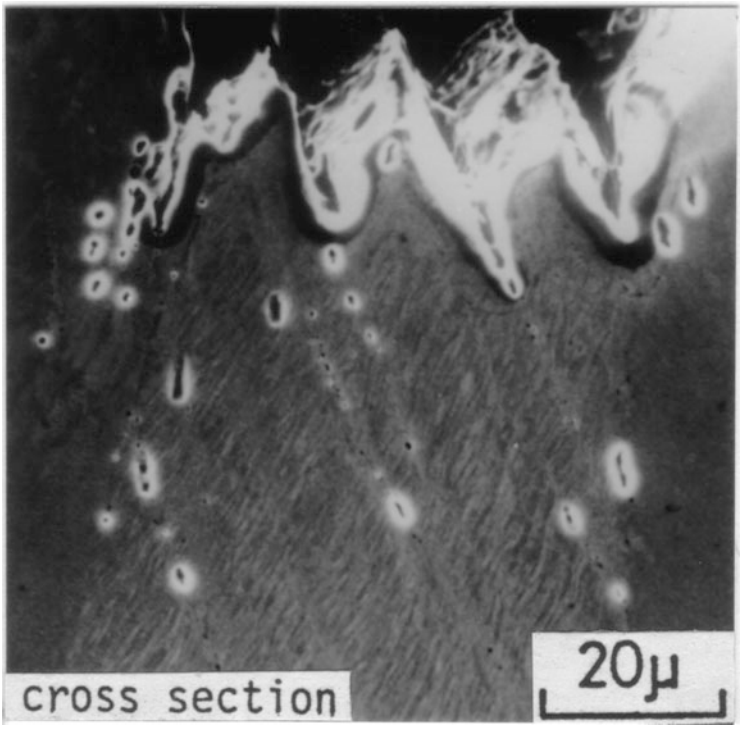


**Fig. 7.3** Cross-sectional view of the area beneath the fracture surface of a coarse-grain iron specimen tensile-fractured under hydrogen charging. The surface striations correspond to internal slip bands and etch pits are formed along slip bands (Nagumo et al. [13])

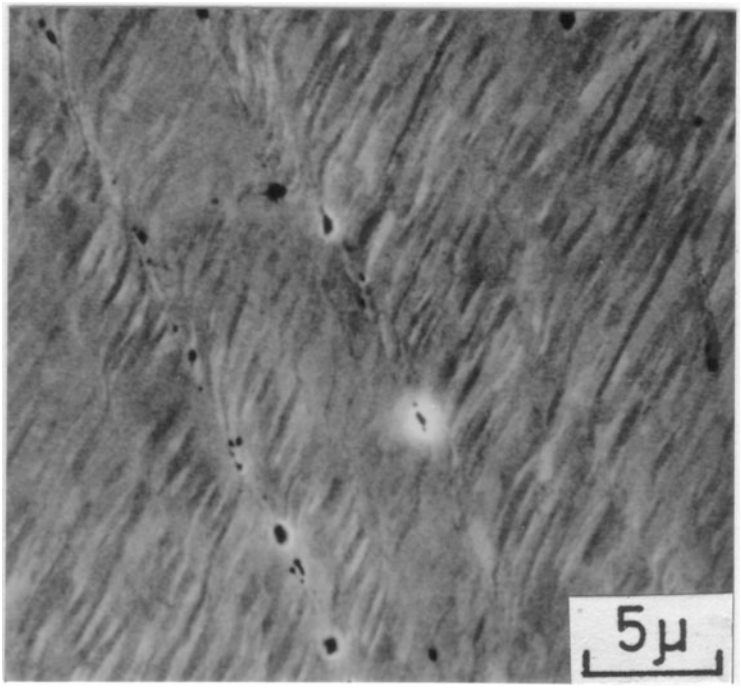


**Fig. 7.4** Etch pits and microvoids formed in deformation bands in a coarse-grain iron specimen tensile-fractured under hydrogen charging (Nagumo et al. [13])

bamboo structure and fracture took place after the onset of necking. Striations on the fracture surface were coarse and corresponded to internal deformation structures. Striations were on the extension of deformation bands in which etch-pits and microvoids were formed as shown in Fig. 7.4 [13].

Trace analyses showed that lamellae in Fig. 7.4 are coincident with {110} and {112} slip planes. Deformation bands are regions where slip on the primary slip planes is hindered by the activation of secondary slip, thus causing there a high dislocation density resulting in mutual interactions of dislocations. TEM observations near the fracture surface revealed the formation of dislocation cell structures with cell walls coincident with {112} traces [13]. The formation of etch-pits implies deterioration of crystallinity at the sites. It is a natural consequence that the sites of intense strain localization act as void nucleation sites and that the voids link along deformation bands in the MVC process. The continuity of steps on the fracture surface to internal slip bands and the crack formation along active slip bands were also reported with hydrogen-charged austenitic stainless steels subjected to tensile fracture [14]. Hydrogen diffusivity in austenite is very low and the void formation is hardly ascribed to the precipitation of molecular hydrogen during the test. Fracture morphologies of austenitic stainless steels are described in Sect. 8.4.3.

(d) Quasi-cleavage

"Quasi-cleavage" is a term that broadly indicates fracture surfaces fairly flat and with irregular markings on planes not specified to cleavage planes. Quasi-cleavage (QC) is often observed for hydrogen embrittlement of steels and the morphology differs by microstructures, specimen geometries and also by hydrogen-charging conditions.

The fracture surface of a low carbon tempered martensitic steel (0.06C-5.9Ni-1.2Mn-0.7Cr-0.2Mo) subjected to three-point bending after hydrogen charging exhibited irregular flaky patterns of about 10 μm in size [15]. The specimens were a fatigue-notched standard Charpy type, and hydrogen precharging was conducted by cathodic electrolysis under a fairly high fugacity in poisoned 1 N $H_2SO_4$ at a current density of $10^3$ A/m$^2$. Scanning electron micrograph revealed fine, lath-like features that correspond in dimension to martensite laths. The shape of etch-pits on the surface revealed their formation on {110} surfaces. The TEM observations also revealed that the fracture surface was along martensite lath boundaries almost over its whole length. The lath boundaries are sites of high dislocation density. The observations also revealed many fine secondary cracks immediately beneath the fracture surface and their initiation at irregularities in the lath boundary such as boundary intersections, steps or foreign particles.

Quasi-cleavage surfaces which are likely a premature dimple fracture are often observed for medium strength steels and for moderately embrittled high strength steels. Figure 7.5 [16] compares fracture surfaces of a low carbon ferrite-pearlite steel subjected to three-point bending tests with and without hydrogen-precharging. Hydrogen-charging under mild fugacity was conducted by cathodic electrolysis in

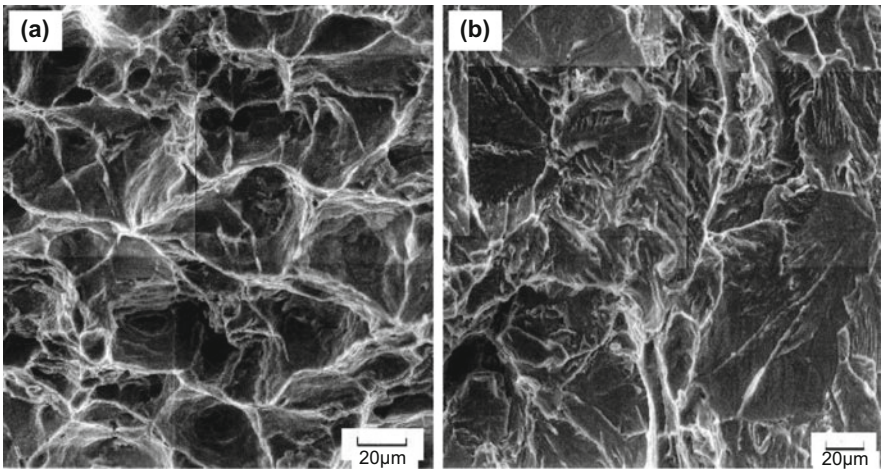


**Fig. 7.5** Fracture surfaces of a low carbon ferrite-pearlite steel subjected to three-point bending tests (**a**) without and (**b**) with hydrogen precharging. (**a**) dimple and (**b**) quasi-cleavage patterns. Hydrogen charging is conducted by cathodic electrolysis in 3 % NaCl + 3 g/*l* $NH_4SCN$ at a current density of 5 A/m$^2$ (Shimomura et al. [16])

3 % NaCl + 3 g/*l* $NH_4SCN$ at a current density of 5 $A/m^2$. Detection of the onset of the stable crack in the steel is shown in Fig. 6.12. Dimple patterns observed for the uncharged specimen changed to QC with irregular morphologies for hydrogen-charged specimens. Fine striations also appeared in the latter. Effects of hydrogen are reasonably ascribed to cause premature fracture before a substantial growth of voids to form round dimples. The reduced roughness of the fracture surface by hydrogen shown in Fig. 7.5 is consistent with the decrease in the crack growth resistance by hydrogen shown in Fig. 6.14 for a low carbon ferrite-pearlite steel of similar compositions.

Microstructural changes that make up QC fracture surface were investigated by means of a focused ion beam (FIB) technique. Martin et al. examined correspondence between fine topographic features and underlying microstructures of API X60 and X80 pipeline steels subjected to compact tension tests in high pressure (5–100 MPa) hydrogen gas [17, 18]. The fracture surface exhibited some different morphologies and the surface with striations was referred as QC. A topographic surface map showed that striations running approximately parallel to the crack direction were in fact ridges. At low magnifications, ridges on quasi-cleavage [17] and fine undulations on flat featureless regions [18] were correlated with intense and highly localized shear bands. In high magnifications, the undulation was composed of small ~50 nm rounded mounds with a high density of dislocation lines and loops immediately beneath the surface [18].

Similarly, the fracture surface of a medium carbon high-strength martensitic steel which was gaseous hydrogen-charged and subjected to four-point bending tests showed "flat" and "quasi-cleavage" features [19]. The maximum nominal bending stress decreased by hydrogen from 2415 MPa to 501 MPa at room temperature. A high density of dislocations with localized slip bands was revealed beneath both "flat" and "quasi-cleavage" features, while flat one was along prior austenite grain boundaries with destructed lath boundaries.

Martin et al. postulated that undulations and mounds on the fracture surface were formed by either near-surface relaxation after fracture or the underlying dislocation structures [18]. However, Lynch objected that mounds were possibly small, shallow dimples resulting from nanovoid coalescence during fracture process [20]. Careful examinations of fracture surfaces were successively conducted by Neeraji et al. for hydrogen-precharged X65 and X80 line-pipe steels [21]. Evolution of a high dislocation density beneath quasi-cleavage facets was consistent with the observations by Martin et al., but mottled contrasts on the fracture surface were confirmed to be nanoscale dimples, 5 ~ 20 nm wide and 1 ~ 5 nm deep, of "valley-on-valley" type by mating halves of conjugate fracture surfaces. The findings indicate that nanovoid nucleation and linking, rather than the separation due to dislocation pileup, have taken place preceding the final fracture.

Quasi-cleavage and striations that characterize fractographic features of hydrogen embrittlement of steels originate in intense strain localization at shear bands. Shear localization promoting final fracture is described in Sects. 7.2.2 and 10.1.3 about the mechanism of hydrogen embrittlement.

(e) Intergranular fracture

Fracture surfaces of hydrogen-degraded high strength martensitic steels often exhibit morphologies that match prior austenite grains. The features have been assigned to intergranular (IG) crack propagation along prior austenite grain boundaries and have served as a basis of brittle fracture models of hydrogen embrittlement. The IG fracture is the typical mode for temper embrittlement of martensitic steels. As for hydrogen effects, a step-cooling heat-treatment of HY 130 (900 MPa in the yield stress) steel drastically reduced the threshold stress intensity for no failure at edge-notched cantilever bend tests in poisoned 0.1 N $H_2SO_4$ using precracked specimens [22]. The slow crack growth in unembrittled specimens started showing fractographic features with some IG mode. The features soon shifted to a mixture of cleavage and MVC and then to fully cleavage in the fast fracture region. On the other hand, embrittled specimens exhibited IG fracture from the point of the crack initiation through the slow and the fast growth regions. Related results for the effects of impurity segregation in prior austenite grain boundaries on hydrogen embrittlement are described in Sect. 8.2.

The IG fracture surfaces are not quite smooth, but usually exhibit fine markings associated with plastic deformation. Hydrogen precharged AISI 4340 steel subjected to sustained-loading tests using compact tension specimens exhibited fracture surfaces mixed of IG, QC and MVC regions [23]. Hydrogen pre-charging was conducted by cathodic electrolysis in poisoned 5 % $H_2SO_4$ at a current density of 20 A/m$^2$, and the crack growth behaviors at the test are described in Sect. 6.2.2 (b).

Main fractographic features of specimens tempered at 230 °C were IG and QC, and the fraction of IG increased by elevating test temperatures from −20 °C to 117 °C. On IG facets, "brittle" striations appeared perpendicularly to the local crack growth direction. The striations occasionally accompanied some small tear ridges, and the spacing of striations was nearly coincident with the average martensite lath spacing of 1 μm. Gerberich et al. assumed that brittle striations were intermittent arrest lines of advancing IG crack. The appearance of IG was less ductile than QC. However, the increase in the areal fraction of IG by elevating test temperatures was against an expected increase in ductility associated with thermal activation of dislocations. As the origin of IG at elevated temperatures, Gerberich et al. noticed a few oxysulfides revealed on IG surfaces. The particles were not associated with ductile tear and were assigned to the brittle fracture initiation sites.

On the other hand, fractographic features for 450 °C tempering showed intermittent slow and fast growth regions accompanying mixtures of IG and MVC ductile rupture regions. The fraction of IG *vs*. MVC was nearly 55 at room temperature. Ductile fingers or ligaments alternated in IG regions with the distance in between about 200 μm. A series of second phase particles was present on IG facets along ductile tearing striations. It was deduced that IG fracture proceeded from the particles in regions 100–200 μm in extent and then destabilized the ligaments to tear by MVC.

The IG fracture surfaces accompanying plasticity are not specific to steels and to the presence of hydrogen. Fracture surfaces of ultra-high strength 7075 aluminum alloys containing high Mg and Zn solutes were predominantly IG mode at fracture toughness tests, and fracture toughness decreased accompanying increasing amounts of IG fracture [24]. High magnifications of IG surfaces revealed very shallow dimples with fine particles ( ~0.1 μm). In situ observations for thin foil specimen revealed void initiation at grain boundary precipitates. It was postulated that the void initiation was induced by constraint against deformation near grain boundaries.

The prevalence of IG mode fracture was demonstrated for compositional effects in medium carbon martensitic steels at slow-elongation rate tensile tests under concurrent hydrogen charging [25]. The compositions of the steels were similar except manganese contents of 0.5, 1.0 and 1.5 %, and the specimens were plates of 2 mm in thickness and 10 mm in width without notch. Hydrogen charging was conducted by cathodic electrolysis in a 3 % NaCl aqueous solution containing 0.5 g/*l* 32# $NH_4SCN$ at a current density of 5 $A/m^2$. Fracture surfaces are shown in Fig. 7.6 [25], and the tensile properties with and without hydrogen charging are shown in Fig. 8.8 in Sect. 8.2. It is to be noticed that enhanced degradation by higher manganese contents appeared only when hydrogen was present.

Fracture under hydrogen-charging always initiated near the corner of the specimen with IG fracture mode prevailing. Fine tear patterns were frequently observed on IG surfaces but the surface was smoother for higher manganese contents. Chemical etching of the IG surface with saturated picral revealed that tear took place along martensite lath boundaries. The average roughness of the fracture surface measured by means of scanning laser microscopy decreased with increasing Mn contents as shown in Fig. 7.7 [25]. The roughness corresponds to the dissipation of plastic energy on crack growth and the results of Fig. 7.7 are in accord with the

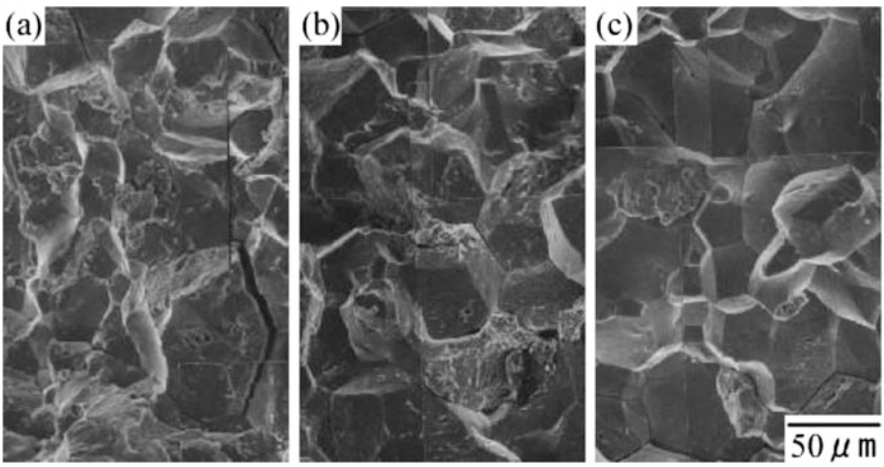


**Fig. 7.6** Tensile-fracture surfaces of medium carbon martensitic steels under hydrogen charging. Manganese contents: (a) 0.5, (b) 1.0 and (c) 1.5 % (Nagumo et al. [25])

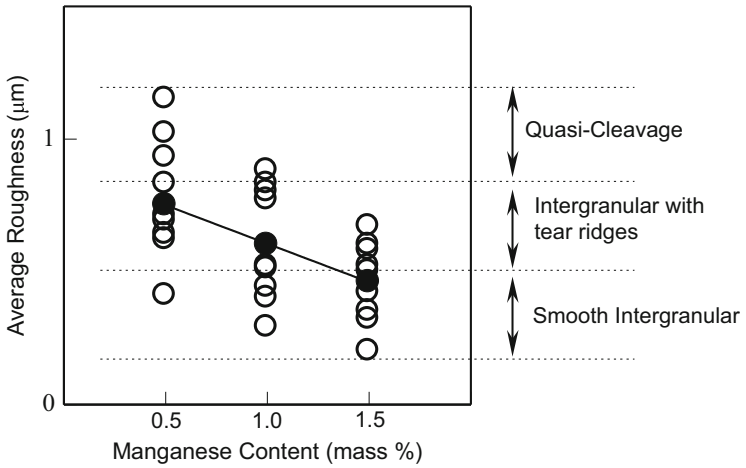


**Fig. 7.7** Average roughness and patterns of fracture surfaces shown in Fig. 7.6 (Nagumo et al. [25])

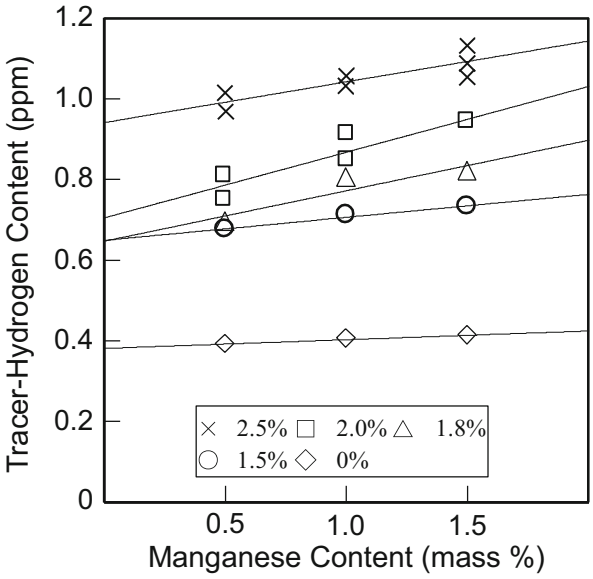


**Fig. 7.8** The amounts of hydrogen absorbed to saturation in specimens given various amounts of prestrain. The three martensitic steels with different Mn contents are used for Figs. 7.6 and 7.7 (Nagumo et al. [25])

pronounced degradation of tensile properties shown in Fig. 8.8 with increasing Mn contents.

A crucial issue concerning IG fracture is the involvement of plasticity in embrittlement. A useful tool to detect lattice defects is to utilize tracer-hydrogen as shown in Figs. 3.2 and 6.25. Figure 7.8 [25] shows the amounts of hydrogen absorbed to saturation in specimens given various amounts of strain. The amount of absorbed tracer-hydrogen represents the densities of trap sites. The amounts for the

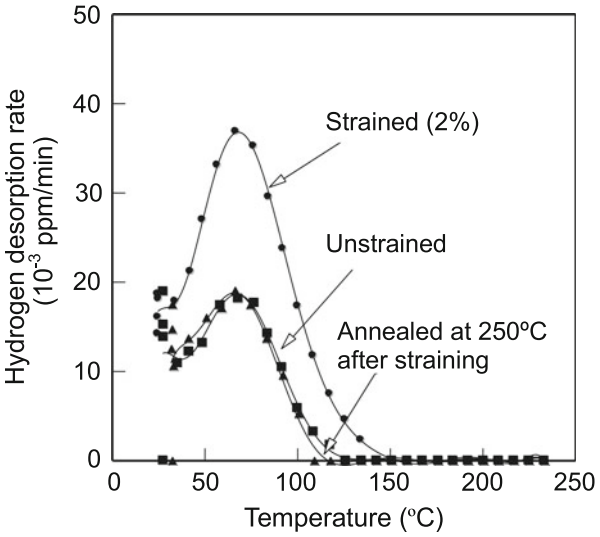


**Fig. 7.9** Thermal desorption profiles of tracer-hydrogen introduced to the steel 1.5 % Mn steel specimens, unstrained, prestrained to 2 % and annealed at 250 °C for 1 h after straining (Nagumo et al. [25])

three steels are almost the same when straining was not given. On the other hand, a substantial increase by straining appeared more pronouncedly for higher manganese contents. As described for Figs. 3.2 and 3.10, TDA is a useful tool to examine the nature of strain-induced defects. Figure 7.9 [25] shows TDA curves of tracer-hydrogen introduced into three states of the 1.5 % Mn specimens, *i.e.* unstrained, prestrained to 2 % and annealed at 250 °C for 1 h after straining. The increase in the amounts of tracer-hydrogen totally disappeared by annealing the strained specimen at temperatures as low as 250 °C, indicating that lattice defects that interact with tracer-hydrogen are vacancies rather than dislocations. Thus, the origin of the effect of manganese contents is reasonably ascribed to the density of strain-induced vacancies. Precipitation of carbides along martensite boundaries was observed, but quantitative differences of microstructures that specify the three steels were not definite. Related degradations of tensile properties are described in Sect. 8.2.

Related information was reported from X-ray diffraction line broadening on IG fracture surfaces [26]. Fracture surfaces of compact tension test specimens of hydrogen-precharged 3.5 % Ni martensitic steel specimens showed IG fracture mode. Doping of phosphor and coarsening of prior austenite grain size reduced the threshold stress intensity and increased the crack growth rate. Rough and striped grain facets on fracture surfaces of undoped specimens became smoother and featureless by phosphor doping and grain coarsening. The {110} X-ray line was broader for the smooth surfaces than for the rough surfaces. It indicates the existence of a larger amount of residual strain beneath the fracture surface while plasticity is apparently less on the fracture surface. The relation between the fracture surface and X-ray line broadening is consistent with the findings in Figs. 7.7 and 7.8.

(f) Effects of stress and hydrogen concentration

Fractographic features are not uniform over the entire crack path. The propagation of a pop-in crack introduced by wedge-loading of AISI 4340 steel specimens in 3.5 % NaCl solution under a freely corroding (stress corrosion cracking, SCC) or attached to Mg anode (hydrogen assisted cracking, HAC) condition showed transitions of the fracture surface in a sequence of ductile dimple, QC, IG and fast fracture [27]. The test was a decreasing stress intensity ($K$) type during the crack growth. Beachem postulated that dissolved hydrogen enhanced deformation and that the crack path was determined by $K$, the dissolved hydrogen content $c_H$, and the microstructure. The combination of $K$ and $c_H$ at the crack tip varies with time. Beachem proposed a qualitative diagram of critical combinations of $K$ and $c_H$ for each fracture mode [27]. According to the diagram, the decrease in $K$ at a constant $c_H$ or in $c_H$ at a constant $K$ results in changes of the fracture modes as MVC → QC → IG. The diagram was an experimental one and microscopic origins of various fracture modes were not definite.

The change in the fracture mode of cracks from QC to IG was also observed for high strength AISI 4340 and ASTM A490 steels subjected to constant-stress delayed fracture tests [28]. The two steels were 1970 and 1700 MPa in tensile strength, respectively, and specimens were round and V-notched bars, respectively. Concurrent hydrogen charging was conducted by cathodic electrolysis in 1 N $H_2SO_4$ at a current density of 10–1000 A/m$^2$. The length of the QC region increased with decreasing notch sharpness and applied stress level. The results implied that QC triggered IG and that the crucial process for the start of delayed fracture was QC associated with plasticity even though the macroscopic fracture mode was brittle-like IG.

Alternatively, a highly disordered microstructure was revealed on the fracture surface of a hydrogen-charged iron [29]. Plate specimens of a 0.06%C ferritic steel of 310 MPa in tensile strength were tensile fractured under concurrent cathodic hydrogen-charging in 3 % NaCl + 3 g/$l$ $NH_4SCN$ aqueous solution at a current density of 10 A/m$^2$. The hydrogen charging condition was fairly mild and the elongation to fracture was still as large as 19 % in the presence of hydrogen. The fracture surface and the subsurface area were examined by TEM observations using a FIB technique for the sample preparation. The selected electron diffraction (SAD) from the fracture surface showed halo patterns and the lattice image of the surface layer showed disordered distributions of atoms. The thickness of the layer was less than 1 μm and the dislocation densities in neighboring areas were very high forming cell structures. Similarly disordered, amorphous-like layers of about 50 nm in thickness were also occasionally observed along dislocation cell walls at about 1 μm below the fracture surface.

In above experiments, many short cracks were present transverse to the tensile axis on the side surface of the fractured specimens. Similarly to the subsurface area, a featureless zone existed in the crack front as shown in Fig. 7.10 [29]. The SAD pattern in the insert showed halo rings similar to that at the subsurface, and dark

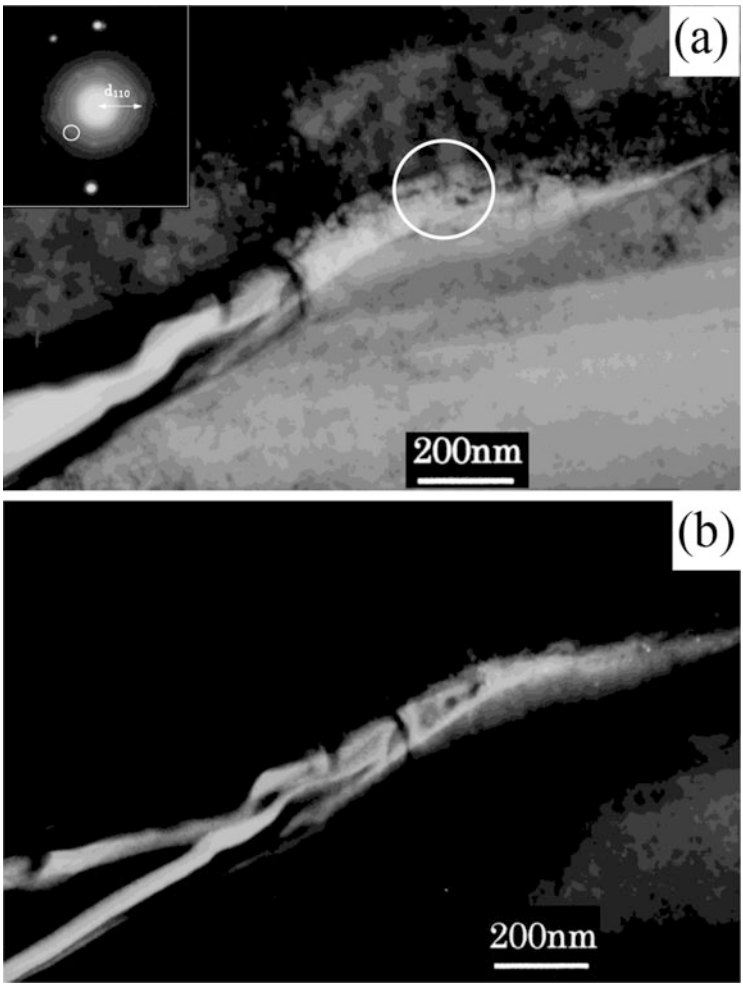


**Fig. 7.10** (**a**) Featureless zone revealed by transmission electron microscopy in front of a small side crack formed on an iron specimen tensile-fractured under concurrent hydrogen-charging. (**b**) The dark field image of the encircled area in (**a**) from a hallo ring in selected electron diffraction (Nagumo et al. [29])

field image clearly showed the presence of amorphous-like structures in the crack front. The featureless zone of a few 100 nm in length was within the plastic zone.

Solid state amorphization induced by heavy plastic deformation has been known with mechanical alloying. The mechanical property of amorphous metallic alloys is characterized by low strain hardening that promotes strain localization and plastic instability. Hydrogen drastically reduces ductility of amorphous metals accompanying volume expansion [30]. Heavily disordered microstructures shown in Fig. 7.10 are in accord with high densities of vacancies suggested by the HESIV

mechanism [8]. [25], and are viable as the origin of reduced ductility. However, only limited observations have been reported on the formation of amorphous phase at hydrogen embrittlement.

## 7.2 Strain Localization and Plastic Instability

### *7.2.1 Strain Localization*

(a) Surface morphology

Fractographic features such as shallow dimples and QC in hydrogen embrittlement suggest that hydrogen suppresses the extension of plastic deformation on crack propagation. Hydrogen-enhanced strain localization has been reported often with slip morphology. Straightening, coarsening and increasing height of slip steps in the presence of hydrogen have been observed on fracture surfaces and side surfaces of tensile fractured austenitic stainless steel foil specimens [14, 31]. Confined surface reliefs along the advancing fatigue crack for a bulky specimen of hydrogen-precharged Type 304 stainless steel are shown in Fig. 7.11 [32]. Hydrogen was thermally precharged to about 90 mass ppm in high pressure hydrogen gas and the fatigue test was tension-compression at stress ratio of −0.1 and at frequency of 1.0 Hz. A small hole was drilled on the surface of specimens as the crack starter.

The features likely result from movements of dislocations taking different slip systems. For austenitic stainless steels, the primary factor that promotes the planarity of slip is stacking fault energy. For fcc metals and alloys, stacking fault energy plays a crucial role in plastic deformation associated with the ease of cross-slipping. Hydrogen reduces stacking fault energy and reported reductions are from 18 ~ 15 mJ/m$^2$ to 12 mJ/m$^2$ by 12 mass ppm of hydrogen and from 34.2 mJ/m$^2$ to 27.7 mJ/m$^2$ under 5.3 kPa of hydrogen gas for a Type 304 austenitic steel [33] and for a Type 310S austenitic steel [34], respectively. Effects of alloying elements on stacking fault energy in austenitic stainless steels were calculated by a first-principles calculation [35].

However, other types of steel also showed enhanced slip localization by hydrogen. Localized deformation around the advancing fatigue crack similar to Type 304 was observed for high strength Cr-Mo martensitic steel subjected to tension-compression fatigue tests [36]. Specimens were hydrogen-charged by immersion in 20 % $NH_4SCN$ aqueous solution at 40 °C. Compared to hydrogen-uncharged specimens, the fatigue crack growth was straighter and slip bands were more concentrated near the crack front.

The effects of hydrogen on the morphology of slip bands were examined precisely for a 0.45 % C steel with ferrite and pearlite structures subjected to rotational bending fatigue tests at 45 Hz using shallow notched specimens hydrogen-precharged by immersing specimens in 20 % $NH_4SCN$ aqueous solution at 40 °C [37]. Morphologies of slip bands at the notch root were examined using a

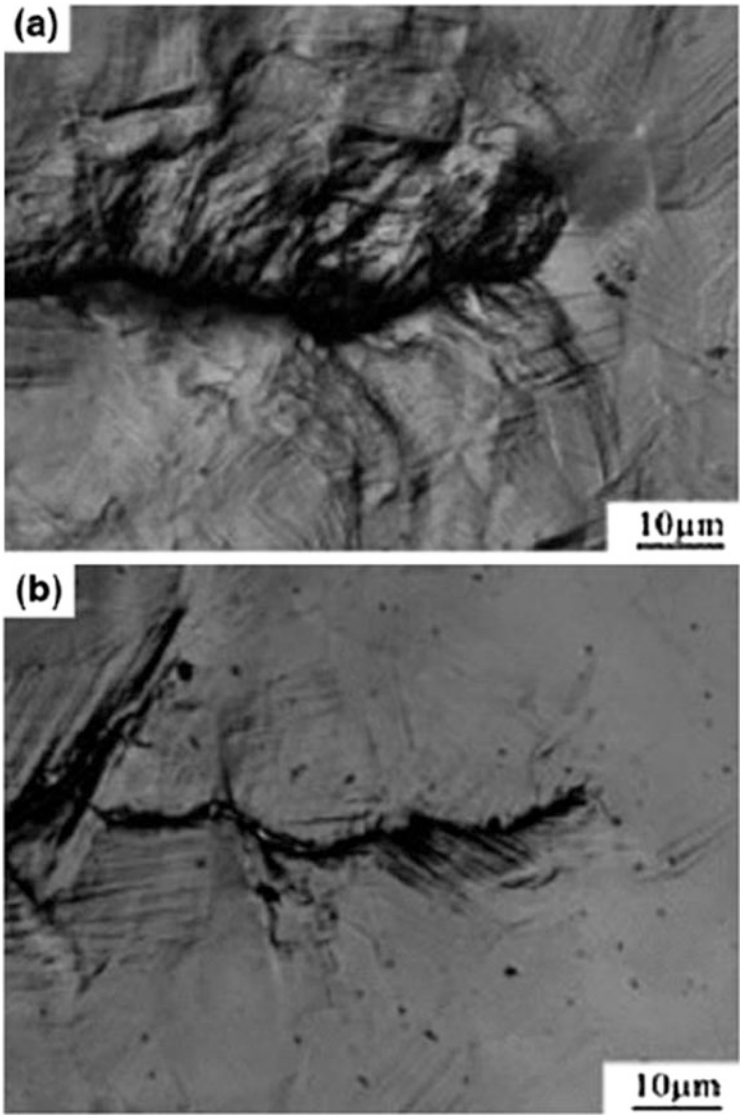


**Fig. 7.11** Slip deformation behaviors near fatigue crack in Type 304. (**a**) Uncharged, $N = 13{,}200$, (**b**) Hydrogen-charged to 47.2 mass ppm, $N = 18.4000$ (Murakami et al. [32])

laser microscope for replicas of microstructures and were classified into three types as illustrated schematically in Fig. 7.12 [37]. The fraction of ferrite grains of Type C with discrete localized slip bands were 49 % in hydrogen-charged specimens after $6 \times 10^5$ fatigue cycles at 230 MPa, while Type C were not observed in uncharged specimens. Also, about 20 % of the crack initiation sites were along slip bands in hydrogen-charged specimens, while almost all were at grain boundaries in

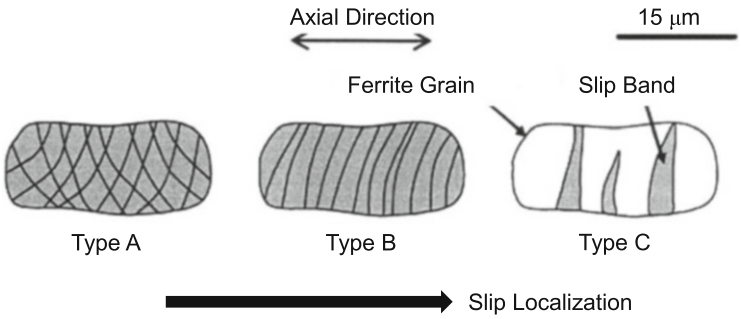


**Fig. 7.12** Schematic illustrations of three types of slip bands at the notch root on 0.45 % carbon ferrite-pearlite steel specimens subjected to rotational bending fatigue (Uyama et al. [37]. Reprinted with permission from John Wiley & Sons)

uncharged ones. The results demonstrated hydrogen-enhanced slip localization and the crack nucleation therein. Degassing by aging hydrogen-charged specimens at room temperature for 270 h substantially reduced the fraction of Type C grains after fatigue tests.

Intense slip bands act as crack initiation sites as revealed in Fig. 7.3. Surface cracks at U-notch bend tests of spheroidized AISI 1090 steel specimens appeared at intense surface rumpling induced by slip bands [38]. The situations were essentially similar between hydrogen-charged and uncharged specimens, but a similar level of surface roughness or cracking was brought about for hydrogen-charged specimens by strain of about a factor of two lower than uncharged ones [38]. A similar U-notch bend test was conducted for quenched and tempered AISI 4340 steel of 1.35 MPa in tensile strength with and without hydrogen precharging under a high hydrogen fugacity estimated to be 1GPa [39]. Strain to fracture was markedly reduced by hydrogen-charging and cracks nucleated internally in a mode I manner. The crack extension to the surface was along the characteristic slip path. Concurrent hydrogen charging, instead of precharging, markedly promoted the crack nucleation reducing the plastic strain for the nucleation to essentially zero.

(b) Internal structures

Observations of deformation microstructures around fatigue crack by high-voltage electron microcopy (HVEM) were reported for Fe-2.6%Si single crystalline specimens [40]. The fatigue test was a sinusoidal tensile loading in hydrogen or helium gas of 0.58 MPa at stress ratio of 0.1 and 1 Hz in frequency. The crack propagation was along the $(1\ \bar{1}\ 0)$ plane in the [001] direction. Cross-sections of specimens exhibited remarkably different morphologies of slip and the crack outline between tests in hydrogen and helium gases. In hydrogen gas, the crack tip was sharp and the distribution of slip bands was concentrated within 5 μm from the crack, consistently with the surface relief observed for austenitic steels [32]. Also important is that the immediate vicinity of the crack was severely deformed while the crack outline was “brittle-like” straight. Slip bands were

intermittently emitted from the crack tip, corresponding to the macroscopic crack growth rate.

The findings indicate that the crack advance is facilitated by extremely localized strain at the crack tip prior to the extension of the plastic region that accompanies the macroscopic crack opening. However, which of enhanced strain localization itself or associated creation of defects is the primary function of hydrogen in the crack advance is a matter to be examined further in Sect. 7.3.2.

Hydrogen-enhanced strain localization in internal microstructures was also revealed in addition to surface morphologies for austenitic stainless steels. Figure 7.13 [8] shows kernel average misorientation (KAM) maps obtained from electron backscatter diffraction (EBSD) for Type 304 austenitic stainless steels

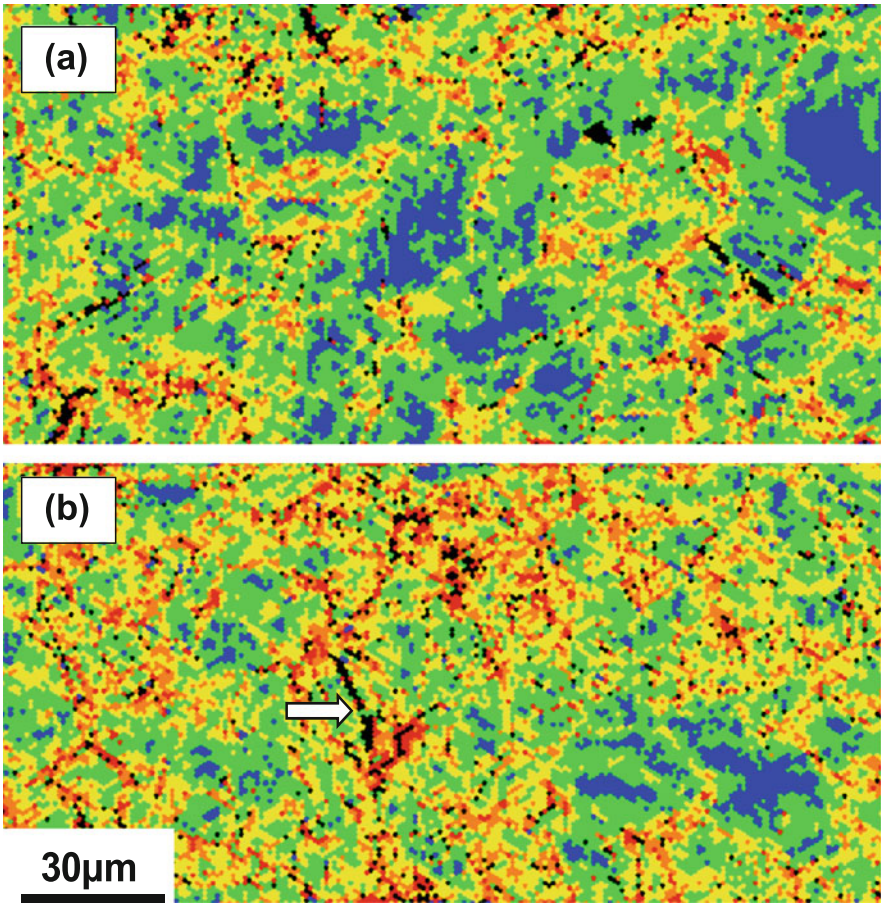


**Fig. 7.13** Kernel average misorientation (KAM) maps of EBSD for Type 304 austenitic stainless steels tensile strained to 24 % (**a**) without and (**b**) with hydrogen precharging. Blue to red denotes higher misorientations between neighboring pixels. The *arrow* in (**b**) indicates annealing twin boundary (Hatano et al. [8])

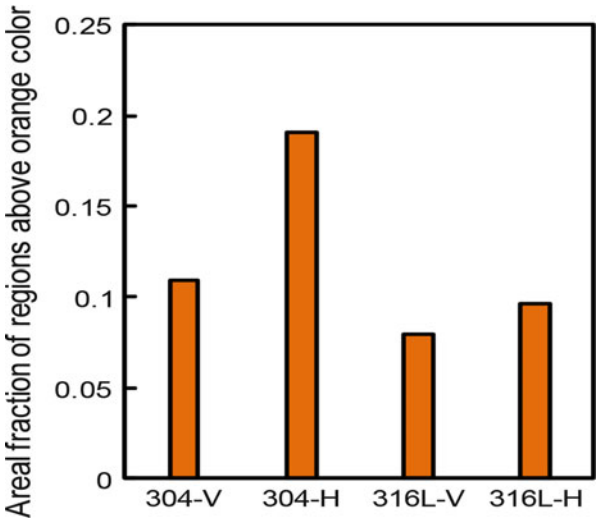


**Fig. 7.14** Areal fractions of highly strained regions of orange and red colors in Fig. 7.13. Data for Type 316 L are also added. Suffixes "V" and "H" denote without and with hydrogen charging, respectively (Hatano et al. [8])

tensile strained to 24 % at room temperature with and without gaseous hydrogen precharging conducted under a high pressure at elevated temperature. The KAM map represents orientation differences between neighboring pixels and is a measure of the amount of strain. Blue to red colors in the KAM maps denote five levels from 0 to 5°.

The strain distribution is not uniform, and increased areal fractions of bright (orange and red) regions imply enhanced strain localization. A substantial decrease in tensile ductility by hydrogen appeared in Type 304, while Type 316 L was immune to hydrogen. Enhanced strain localization by hydrogen was observed also for Type 316 L, but it was to a less extent compared to Type 304. Figure 7.14 [8] shows a quantitative comparison of strain localization in terms of area fractions of orange and red color regions for Types 304 and 316 L steels strained to 24 % with and without hydrogen charging. Evidently the hydrogen effect to enhance strain localization is much more distinct in Type 304 than Type 316 L. The preferential strain localization in Type 304 is ascribed to stacking fault energy. The decrease in the stacking fault energy enhances strain-hardening and resultant phases such as stacking fault and $\varepsilon$-martensite act as barriers for the extension of slip. High densities of fine stacking faults and streaks of $\varepsilon$-martensite characterize microstructures of hydrogen-charged and deformed Type 304 austenitic steel [8]. Deterioration of crystallinity associated with strain localization is described in following Sect. 7.3.

Concurrently conducted positron annihilation spectroscopy (PAS) exhibited a more prominent increase in the mean positron lifetime associated with straining for Type 304 than for Type 316 L [8]. The utilization of PAS for identifying the type of hydrogen-enhanced strain-induced lattice defects is described in Sect. 3.2.3(b). For iron, isochronal annealing showed that the effect of hydrogen on increasing positron lifetime is due to the enhanced creation of vacancies. For austenitic stainless

steels, vacancy clustering proceeded more prominently in Type 304 than in Type 316 L. The effects of enhanced strain localization on hydrogen embrittlement are related with enhanced creations of vacancies and their clusters. Other possibilities such as buildup of high local concentrations of hydrogen are not feasible because of very low diffusivity of hydrogen in austenitic stainless steels. Strain-induced transformation to martensite was not detected even in a region about 0.5 mm from the fracture surface of Type 304 [8].

### *7.2.2 Plastic Instability*

Plastic instability is the localization of plastic flow departing from a homogeneous deformation during stressing process [41, 42]. Flow localization into a shear band appears as void sheet linking [43]. Plastic instability appears in uniaxial straining when the cross-section of a small portion of the length of the specimen differs from that of the remainder and the magnitude of the difference increases in the course of straining. Plastic instability is a crucial process in ductile fracture, and its mechanistic significance for ductile fracture is described in Sect. 10.1.3.

The appearance of rugged surface shear bands at U-notch bend tests of spheroidized AISI 1090 steel indicated the onset of flow localization or plastic instability [38]. Hydrogen promotes the evolution of surface rumpling and reduces the critical strain for the onset of plastic instability well before the profuse void formation in the bulk [38]. Internal small crack nucleation following surface rumpling was along characteristic slip traces as shown in Fig. 7.15 [38]. Criteria

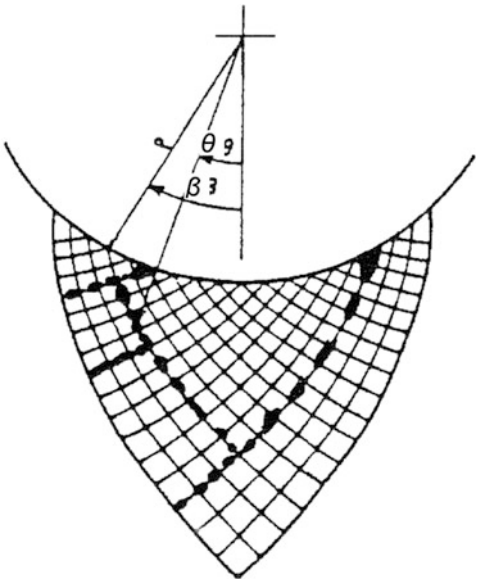


**Fig. 7.15** Schematic show of logarithmic spiral slip traces for circular notch root and the formation microcracks (Onyewuenyi et al. [38])

of the onset of plastic instability are derived from material constitutive relations. The observed critical principal notch surface strain for the onset of plastic instability was in good agreement with the values calculated for a U-notched bend specimen [38]. For a U-notched bend test of AISI 4340 steel, the critical notch root strain at the crack initiation was nearly constant for three different notch-root radii of specimens [39]. It was deduced that hydrogen promoted plastic instability and that the crack nucleation within the plastic zone was induced by a combination of hydrogen concentration and total stress.

A crack initially formed in the central part of the specimen propagated stepwise following a "void sheet" path. Link-up of microcrack with a void situated at the tip of the microcrack by shear was reported for spheroidized AISI 1520 steel bar specimens subjected to axisymmetric tension after hydrogen precharging [43]. In that case, second phase particles were not ruled out as the crack initiation sites, but hydrogen promoted plastic instability and favored crack propagation.

The effects of hydrogen on the mixed mode I/III loading to fracture toughness tests, shown in Fig. 6.10, and the stable crack initiation from the precrack, shown in Fig. 6.13, are likely due to enhanced plastic instability as described in Sects. 10.4 and 10.5.

## 7.3 Precursory Damage to Crack Initiation

Hydrogen embrittlement draws attention when accidents such as delayed fracture of high strength fasteners or leak of sour oil/gas from pipes happen. Most studies so far conducted have remarked the onset and growth of cracks. However, the degradation of materials during the service practice is extremely important in stages preceding the onset of fracture, and the effects of hydrogen on the creation of damage in materials are critical subjects. The term "damage" in engineering often addresses flaws such as cracks or voids, but here it is used in a wide sense addressing crystalline deterioration far below visual scale.

### *7.3.1 Generation of Damage During Mechanical Tests*

Local lattice distortion around hydrogen-induced cracks was detected for pure iron single crystal as smearing of X-ray Kossel lines [44]. Cathodic hydrogen-charging at a current density of 300 A/m$^2$ without external stress produced internal cracks of 50–75 μm in size accompanying lattice distortion localized within 100 μm of cracks. However, distorted absorption conics (Kossel lines) were also observed in regions where cracking had not yet occurred. Broadening of X-ray diffraction line width associated with hydrogen-charging was observed for mild steel specimens cathodically hydrogen-charged in poisoned 0.1 N $H_2SO_4$ at the current density of $10^3$ A/m$^2$ [45]. The line broadening was unchanged during exposure of specimens

at room temperature, but decreased about 25 % at 200 °C and almost totally disappeared at 400 °C. The aging behaviors imply that the line broadening was not due to elastic strain around hydrogen atoms but to plastic deformation induced at the time of hydrogen charging. The aging behaviors are quite consistent with Figs. 3.2(b) and 3.10 that imply vacancy-type defects created by plastic straining.

The effects of hydrogen on inducing lattice distortion are enhanced when plastic straining has been or is simultaneously applied to the specimen. The image quality (IQ) of EBSD analysis represents the crystallinity of the diffracting area and the dark contrast results from lattice distortion. Figure 7.16 [8] shows IQ maps of hydrogen-charged Type 304 austenitic stainless steel given tensile strain of 5 % or 24 %. The maps show more pronounced lattice distortion with increasing strain in regions close to grain-boundaries than in the bulk. The average strain obtained

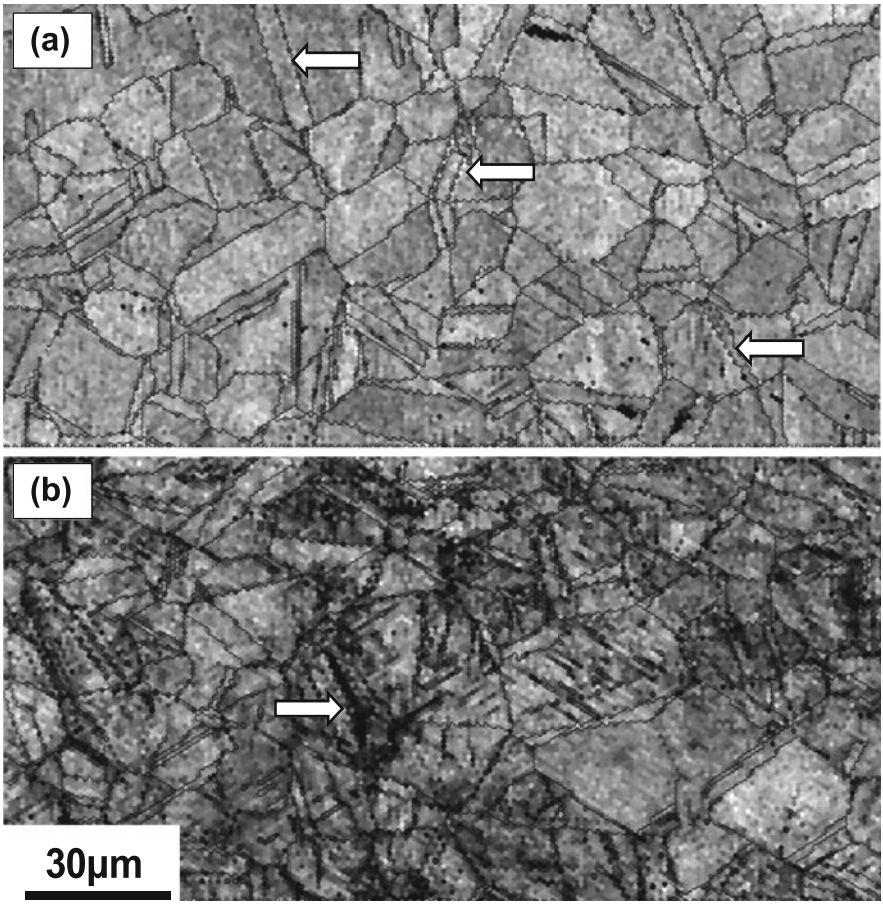


**Fig. 7.16** Image quality (IQ) maps of EBSD for hydrogen-charged Type 304 austenitic stainless steels tensile strained to (**a**) 5 % and (**b**) 24 %. Arrows indicate annealing twin boundaries (Hatano et al. [8])

separately from KAM maps was reasonably lower for the specimen strained to 5 % than that for 24 %, but preferential strain localization appeared in hydrogen-charged Type 304 at strain as low as 5 % [8]. Annealing twins were often observed within grains, as indicated by arrows in Fig. 7.16, and twin boundaries tended to become blurred with increasing strain, implying distortion of areas near the interface of twin bands.

Nibur et al. examined fractographic features and deformation microstructures of 21Cr-6Ni-9Mn austenitic stainless steel specimens subjected to a compact tension test after thermal hydrogen precharging [46]. The features were somewhat dependent on included ferrite volume contents in the material, but the effects of hydrogen-precharging were characterized by shallow, non-equiaxed dimples and flat facets with limited plasticity. Examinations of cross-sections revealed the primary void nucleation at deformation band intersections. Relatively large facets were covered with fine, elongated dimples, and cross-sectional examinations revealed concentrations of microvoids along a continuous obstacle such as another deformation band. For the annealed material, microcracks were revealed along annealing twin boundaries at intersection points with deformation bands. The observations are consistent with the formation of a small crack at the intersection of slip bands shown in Fig. 7.2 for pure iron and the void nucleation in deformation bands shown in Figs. 7.3 and 7.4 for a ferritic steel. Nibur et al. postulated that hydrogen-enhanced localized plasticity (HELP) causes strain discontinuities at obstacles and void nucleation, but the deterioration of crystallinity along twin boundaries shown in Fig. 7.16 for Type 304 steel is also viable as the precursor of void nucleation. Fractographic features and deformation microstructures of austenitic stainless steels are further described in Sects. 8.4.3 and 8.4.4.

Koyama et al. prepared a 0.15 % C ferrite/martensite dual phase (DP) steel by water-quenching from the two-phase region and showed a substantial degradation by hydrogen-precharging on tensile straining [47]. Koyama et al. examined internal microstructures and used the term “damage” for flaws such as cracks and voids. The onset of necking and the evolution of the damage area during straining took place earlier for hydrogen precharged specimens than for uncharged specimens. An IQ map revealed the incipient crack nucleation in the incubation period before a substantial crack growth mostly inside of martensite. The grain-average KAM distributions associated with straining up to 7 % were unaffected by the presence of hydrogen in both ferrite and martensite phases, but incipient cracks grew into neighboring ferrite grains for hydrogen-charged specimens. Changes of the local orientation and high KAM values around the crack tip for hydrogen-charged specimens suggested a reduced crack-arresting ability by hydrogen. Related subjects on DP steels are described in Sect. 8.3.

The creation of lattice defects during incubation periods of fatigue and delayed fracture tests are shown in Figs. 6.17 and 6.25, respectively, detected by means of TDA of hydrogen used as the tracer of defects. The tracer-hydrogen contents in Fig. 6.17 are from the portions close to the fracture surfaces of high strength Si-Cr steel specimens subjected to rotational bending fatigue tests. Using the same test method, the fatigue-cycle dependence of the density of lattice defects was

examined for two martensitic steels, a high strength Si-Cr steel bar designed for spring and a PC steel bar for pre-stressing tendom [48]. The amount of tracer-hydrogen increased in the latter half of fatigue lives for both steels, indicating accumulation of damage preceding the final fracture. The amounts of tracer-hydrogen in fatigued specimens decreased by annealing at 200 °C, indicating the vacancy-type nature of the lattice defects created before fracture. However, changes in the amount of tracer-hydrogen in the incubation stage were not simple depending on the tested steels. Preceding the increase in the late stage of fatigue, the amount of tracer hydrogen gradually decreased with fatigue cycles for PC steel while the decrease was very small for Si-Cr steel. The reason of the decrease and its dependence on steels is not definite, but reconfigurations or annihilation of dislocation structures during cyclic stressing were premised [48].

Positron annihilation spectroscopy (PAS) is another useful tool for detecting damage and was applied to tensile straining of Type 304 steel to identify types of lattice defects enhanced their creation by hydrogen. Figure 7.17 [8] shows mean positron lifetimes $\tau_m$ of Type 304 and Type 316 L steels given tensile straining with and without hydrogen-charging to 30 mass ppm. Hydrogen-charging prominently enhanced the increase in $\tau_m$ with increasing strain. The strain-induced increase in $\tau_m$ implies the creation of lattice effects that have longer positron lifetimes than that in the bulk. Successive isochronal annealing of strained materials showed monotonic reduced $\tau_m$ with increasing annealing temperatures [8]. The decrease in $\tau_m$ by annealing continued to temperatures as high as 1000 K, but the enhanced increase in $\tau_m$ by hydrogen disappeared by annealing at 300 °C. The annihilation temperature corresponds to that of vacancy clusters, and the difference of hydrogen effects between Type 304 and Type 316 L is ascribed to the creation and clustering of strain-induced vacancies. The results are consistent with PAS measurements for iron [49]. However, the observed $\tau_m$ is a weighted average of multiple lifetime components as described in Sect. 3.2.2. The contributions of dislocations and

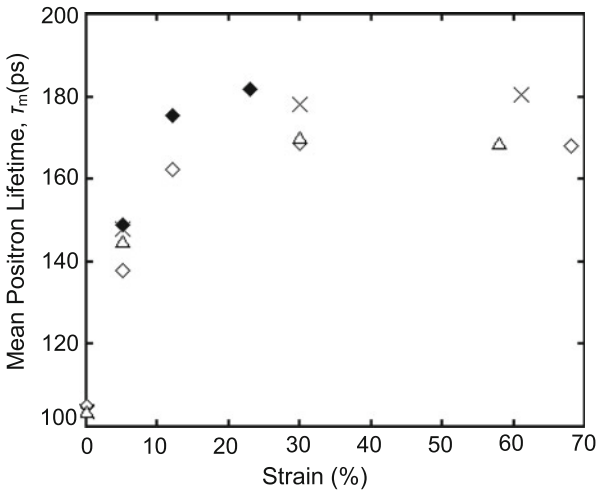


**Fig. 7.17** Mean positron lifetimes of strained austenitic stainless steels: ◇, SUS304; ♦, H-charged SUS304; Δ, SUS316L; ×, H-charged SUS316L (Hatano et al. [8])

vacancies to $\tau_m$ for iron deformed with and without hydrogen-precharging are tabulated in Table 3.4. The deformation microstructures are further described in Sect. 8.4.4.

### 7.3.2 *Effects of Stress History*

Hydrogen degradation is evaluated under various types of loading. Controlling factors differ by the types, and operating mechanisms might not necessarily be identical. Structural components tolerate various stress histories during service, and damage produced in early stages is to be carried over to final fracture if hydrogen effects are common in each stage. In this section, some experiments about the effects of stress histories on hydrogen degradation are presented.

In Sect. 6.1(b), the essential role of vacancy-type lattice defects in hydrogen degradation in tensile tests is presented for iron, cold-drawn eutectoid steel and Inconel 625 alloy. Cyclic variations of applied stress promote failure at sustained-loading delayed fracture tests of martensitic steel as described in Sect. 6.4.3(a). Then, the effects of cyclic prestressing with and without hydrogen on tensile tests were examined for martensitic steel of 1433 MPa in tensile strength with respect to the creation of damage [50]. Initially, the applied stress was cyclically varied in the range of $0.7 \pm 0.1$ of the tensile strength with a triangular form. The strain rates and cycles were varied, and hydrogen-charging was conducted by immersing specimens in 20 % $NH_4SCN$ solution at 50 °C. The specimens pre-stressed with and without hydrogen charging were denoted as $[\sigma + H]$ and $[\sigma]$, respectively. The degradation of tensile properties due to prestressing was expressed in terms of the hydrogen embrittlement susceptibility (*HES*) defined as the ratio of the fracture strain of $[\sigma + H]$ to that of $[\sigma]$ specimens at following tensile tests.

The effects of cyclic prestressing on *HES* are shown in Fig. 7.18 [50] for increasing the numbers of prestressing cycles at various strain rates. The degradation caused by hydrogen was enhanced by cyclic prestressing, more pronouncedly with increasing the number of cycles and reducing the strain rates. Damage introduced by cyclic prestressing was then examined using hydrogen as the tracer. Tracer-hydrogen was charged to saturation into cyclically prestressed specimens after exposing prestressed specimens at 30 °C for 168 h to degas hydrogen introduced at the prestressing stage. Tracer hydrogen was introduced without applying external stress under the same condition as the initial charging.

The amounts of tracer-hydrogen increased with the number of stressing cycles in both $[\sigma]$ and $[\sigma + H]$ specimens and their difference between $[\sigma + H]$ and $[\sigma]$ specimens was denoted as $\Delta C_H$ as a measure of the increase in damage due to hydrogen. The amount of $\Delta C_H$ represents hydrogen effects on the strain-induced creation of defects at cyclic prestressing. The magnitude of $\Delta C_H$ increased with cyclic stressing more pronouncedly with lower strain rates as shown in Fig. 7.19 [50]. The strain-rate dependence is consistent with that for tensile tests shown in Fig. 6.4 in Sect. 6.1(b). It indicates that cyclic stressing accumulates damage

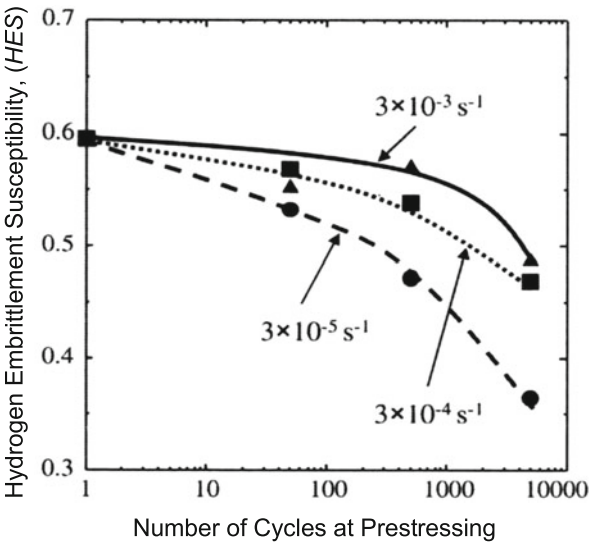


**Fig. 7.18** Hydrogen embrittlement susceptibility (*HES*) on tensile tests of martensitic steel specimens applied cyclic prestressing at various strain rates (Doshida et al. [50])

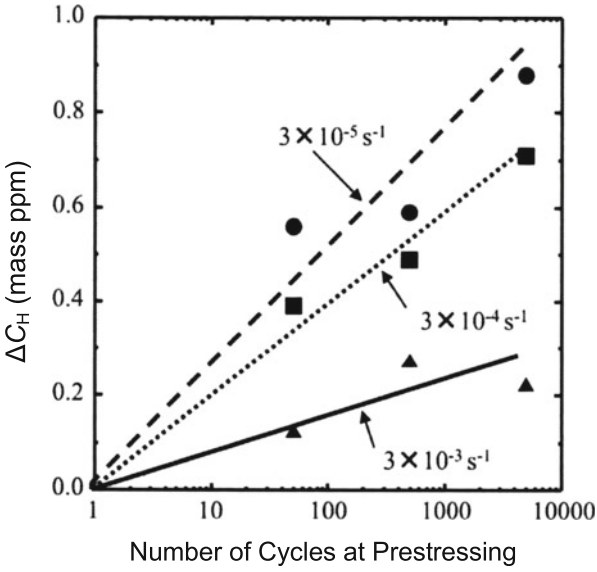


**Fig. 7.19** Hydrogen enhancement of the strain-induced increase in the hydrogen absorption capacity, $\Delta C_H$, on tensile tests of martensitic steel specimens after cyclic prestressing at various strain rates (Doshida et al. [50])

prior to the tensile tests. The thermal desorption profiles of tracer hydrogen showed a single peak centered at about 120 °C, and $\Delta C_H$ humped the higher temperature side of the TDA peak implying vacancy clusters as described in Sect. 3.2.3(b). An approximately linear correspondence exists between *HES* and $\Delta C_H$ [50]. It supports the notion that the hydrogen-enhanced creation of damage causes degradation through the whole stages of deformation.

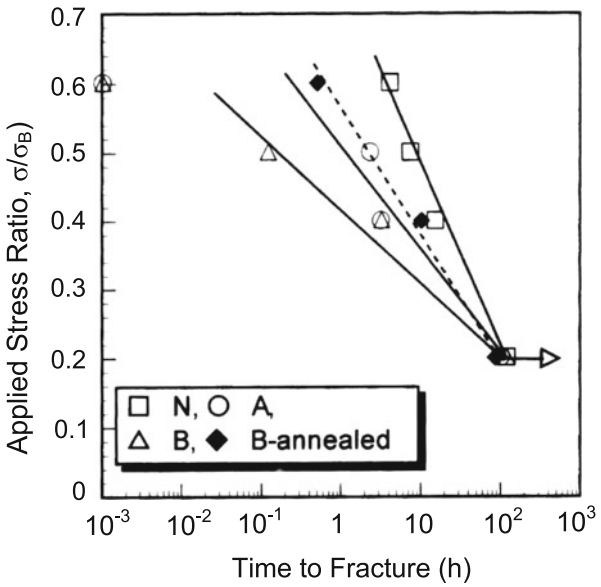


**Fig. 7.20** Delayed fracture diagrams for prefatigued Si-Cr martensitic steel. □, N (without prefatigue); Δ, B (prefatigued close to failure); ◆, B (annealed at 200 °C for 1 h after prefatigue); ○, A (prefatigued to about one half of fatigue life) (Nagumo et al. [51])

In Sect. 6.3(a), promoted fracture by hydrogen at rotational bending fatigue tests of high strength Si-Cr steel is described, and defect creations in early stages of tests before final fracture are shown in Fig. 6.17 [51]. Similarly for delayed fracture, defects are accumulated in the incubation period as shown in Fig. 6.25 for high strength Si-Mn martensitic steel [52]. It leads to an expectation that stress histories play a role in hydrogen degradation.

Figure 7.20 [51] shows promoted delayed fracture by prefatigue for the Si-Cr martensitic steel used for Fig. 6.16. Prefatigue was applied by rotational bending for cycles about a half (Treat-A) of or close (Treat-B) to the fatigue life at the applied stress amplitude level of 640 MPa [51]. The two types of specimens were successively subjected to sustained-loading delayed fracture tests in 20 % $NH_4SCN$ aqueous solution at 50 °C. Specimens without prefatigue (Treat-N) were also tested for comparison. Fracture of specimens given prefatigue for cycles close to the fatigue life, Treat-B, took place substantially earlier. However, annealing of the fatigued specimens at temperature as low as 200 °C for 1 h reduced the degradation caused by prefatigue. The results imply that damage accumulated during prefatigue plays a common function in failure as that created during delayed fracture test and that damage introduced by prefatigue is mostly vacancies without forming flaws such as voids and cracks.

Similar cumulative effects of damage were also shown between delayed fracture and tensile tests for high strength martensitic steel of 1433 MPa in tensile strength [52]. Specimens of 5 mm in diameter were initially sustained-loaded at a constant stress of 80 % of the tensile strength, apparently within the elastic range, for 96 h in 20 % $NH_4SCN$ aqueous solution at 50 °C. After the sustained-loading, hydrogen was completely removed at 30 °C for 168 h and then some specimens were

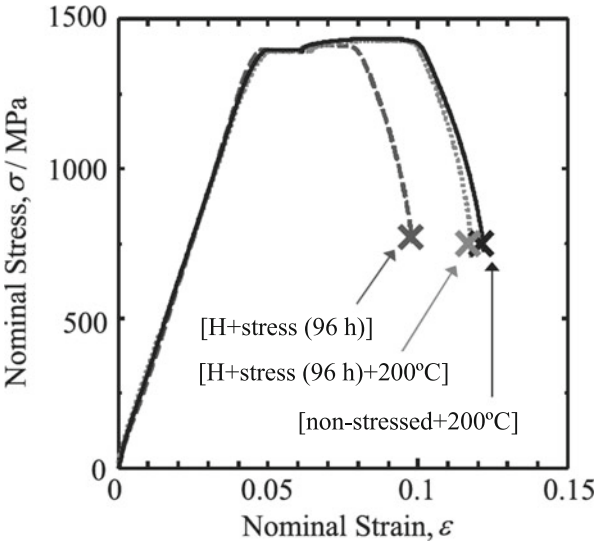


**Fig. 7.21** Tensile curves of high strength martensitic steel specimens. [H + stress (96)]: Initially sustained-loaded in 20 % $NH_4SCN$ aqueous solution for 96 h at 50 °C; [H + stress(96) + 200 °C]: Annealed at 200 °C after sustained loading; [non-stressed + 200 °C]: Annealed at 200 °C without sustained-loading. All specimens are degassed at room temperature before tensile tests (Doshida et al. [52]. Reprinted with permission from The Iron & Steel Inst. Japan)

annealed at 200 °C for 2 h. The two series of specimens are denoted as [H + stress (96 h)] and [H + stress(96 h) + 200 °C], respectively. Also, specimens without sustained-loading but annealed at 200 °C were prepared with the notation of [non-stressed +200 °C]. Stress-strain curves at tensile tests are shown in Fig. 7.21 [52]. It is to be noticed that a substantial degradation appeared for the [H + stress (96 h)] series although hydrogen was absent at the time of tensile testing. The almost complete recovery for the [H + stress(96) + 200 °C] series indicates that the degradation is caused by vacancies created during sustained-loading without forming irreversible voids or cracks.

## References

1. A.S. Tetelman, W.D. Robertson, Acta Metall. **11**, 415–426 (1963)
2. A.S. Tetelman, W.D. Robertson, Trans. Metall. Soc. AIME **224**, 775–783 (1962)
3. F. Terasaki, T. Kawakami, A. Yoshikawa, N. Takano, Rév. Métall-CIT/Sci. Génie Matér. **95**, 1519–1529 (1998)
4. R. Gerber, I.M. Bernstein, A.W. Thompson, Scr. Metall. **10**, 341–345 (1976)
5. J.A. Gordon, J.P. Hirth, A.M. Kumar, N.E. Moody Jr., Metall. Trans. A **23A**, 1013–1020 (1992)
6. M. Nagumo, H. Yoshida, Y. Shimomura, T. Kadokura, Mater. Trans. **42**, 132–137 (2001)
7. S.P. Lynch, Acta Metall. **32**, 79–90 (1984)
8. M. Hatano, M. Fujinami, K. Arai, H. Fujii, M. Nagumo, Acta Mater. **67**, 342–353 (2014)
9. A. Shibata, H. Takahashi, N. Tsuji, ISIJ Int. **52**, 208–212 (2012)
10. M.-J. Lii, X.-F. Chen, Y. Katz, W.W. Gerberich, Acta Metall. Mater. **38**, 2435–2453 (1990)
11. T.J. Marrow, M. Aindow, O. Prangnell, M. Strangwood, J.F. Knott, Acta Mater. **44**, 3125–3140 (1996)

12. F. Nakasato, I.M. Bernstein, Metall. Trans. A **9A**, 1317–1326 (1978)
13. M. Nagumo, K. Miyamoto, J. Jpn. Inst. Metals **45**, 1309–1317 (1981)
14. D.G. Ulmer, C.J. Altstetter, Acta Metall. Mater. **39**, 1237–1248 (1991)
15. Y.H. Kim, J.W. Morris Jr., Metall. Trans. A **14A**, 1883–1888 (1983)
16. Y. Shimomura, M. Nagumo, in *Environment-Induced Cracking of Materials: Chemistry, Mechanics and Mechanisms*", ed. by S.A. Shipilov, R.H. Jones, J.M. Olive, R.B. Rebak (Elsevier, Oxford, 2007), pp. 285–294
17. M.L. Martin, J.A. Fenske, G.S. Liu, P. Sofronis, I.M. Robertson, Acta Mater. **59**, 1601–1606 (2011)
18. M.L. Martin, I.M. Robertson, P. Sofronis, Acta Mater. **59**, 3680–3687 (2011)
19. A. Nagao, C.D. Smith, M. Dadfarnia, P. Sofronis, I.M. Robertson, Acta Mater. **60**, 5182–5189 (2012)
20. S.P. Lynch, Scr. Mater. **65**, 851–854 (2011)
21. T. Neeraj, R. Srinivasan, J. Srinivasan, Acta Mater. **60**, 5160–5171 (2012)
22. K. Yoshino, C.J. McMahon, Metall. Trans. **5**, 363–370 (1974)
23. W.W. Gerberich, T. Livne, X.-F. Chen, M. Kaczorowski, Metall. Trans. A **19A**, 1319–1334 (1988)
24. G.M. Ludtka, D.E. Laughlin, Metall. Trans. A **13A**, 411–425 (1982)
25. M. Nagumo, H. Matsuda, Philos. Mag. A **82**, 3415–3425 (2002)
26. J. Kameda, Acta Metall. **34**, 1721–1735 (1986)
27. C.D. Beachem, Metall. Trans. **3**, 437–451 (1972)
28. H. Yatabe, K. Yamada, E.R. de Los Rios, K.J. Miller, Fatigue Fract. Eng. Mater. Struct. **18**, 377–384 (1995)
29. M. Nagumo, T. Ishikawa, T. Endoh, Y. Inoue, Scr. Mater. **49**, 837–842 (2003)
30. M. Nagumo, T. Takahashi, Mater. Sci. Eng. **23**, 257–259 (1975)
31. D.P. Abraham, C.J. Altstetter, Metall. Mater. Trans. A **26A**, 2859–2871 (1995)
32. Y. Murakami, T. Kanezaki, Y. Mine, Metall. Mater. Trans. A **41**, 2548–2562 (2010)
33. A. Inoue, Y. Hosoya, T. Masumoto, Trans. ISIJ **19**, 170–178 (1979)
34. P.J. Ferreira, I.M. Robertson, H.K. Birnbaum, Mater. Sci. Forum **207–209**, 93–96 (1996)
35. L. Vitos, J.-O. Nilsson, B. Johansson, Acta Mater. **54**, 3821–3826 (2006)
36. H. Tanaka, N. Hommma, S. Matsunaga, Y. Murakami, Trans. Jpn. Soc. Mech. Eng. A **73**, 1358–1365 (2007)
37. H. Uyama, M. Nakashima, K. Morishige, Y. Mine, Y. Murakami, Fatigue Fract. Eng. Mater. Struct. **29**, 1066–1074 (2006)
38. O.A. Onyewuenyi, J.P. Hirth, Metall. Trans. A **14A**, 259–269 (1983)
39. T.D. Lee, T. Goldenberg, J.P. Hirth, Metall. Trans. A **10A**, 439–448 (1979)
40. Y. Takahashi, M. Tanaka, K. Higashida, H. Noguchi, Scr. Mater. **61**, 145–148 (2009)
41. F.A. Nichols, Acta Metall. **28**, 663–673 (1980)
42. O.A. Onyewuenyi, in *Hydrogen Degradation of Ferrous Alloys*, ed. by R.A. Oriani, J.P. Hirth, M. Smialowski (Noyes Pub., Park Ridge, 1985), pp. 414–453
43. I.-G. Park, A.W. Thompson, Metall. Trans. A **21A**, 465–477 (1990)
44. I.M. Bernstein, H.W. Wagenblast, J.L. Bomback, Metall. Trans. **2**, 2533–2534 (1972)
45. K. Kamachi, *Report of Research Team on the Mechanism of Delayed Fracture* (Iron and Steel Institute of Japan, Tokyo, 1975), pp. 93–111
46. K.A. Nibur, B.P. Somerday, D.K. Balch, C. San Marchi, Acta Mater. **57**, 3795–3809 (2009)
47. M. Koyama, C.C. Tasan, E. Akiyama, K. Tsuzaki, D. Raabe, Acta Mater. **70**, 174–187 (2014)
48. M. Nagumo, H. Shimura, T. Chaya, H. Hayashi, I. Ochiai, Mater. Sci. Eng. **A348**, 192–200 (2003)
49. K. Sakaki, T. Kawase, M. Hirano, M. Mizuno, H. Araki, Y. Shirai, M. Nagumo, Scr. Mater. **55**, 1031–1034 (2006)
50. T. Doshida, M. Nakamura, H. Saito, T. Sawada, K. Takai, Acta Mater. **61**, 7755–7766 (2013)
51. M. Nagumo, S. Sekiguchi, H. Hayashi, K. Takai, Mater. Sci. Eng. **344A**, 86–91 (2003)
52. T. Doshida, H. Suzuki, K. Takai, N. Oshima, T. Hirade, ISIJ Int. **52**, 198–207 (2012)